Research Article | Vol. 26, No. 6 | 19 Mar 2018 | OPTICS EXPRESS 7227
Optics EXPRESS

Integration of an InSb photodetector on Si via heteroepitaxy for the mid-infrared wavelength region

Bo Wen Jia,* Kian Hua Tan, Wan Khai Loke, Satrio Wicaksono, and Soon Fatt Yoon

School of Electrical and Electronic Engineering, Nanyang Technological University, 50 Nanyang Avenue, Singapore 639798, Singapore
**jiab0001@e.ntu.edu.sg*

Abstract: In this study, InSb p-i-n photodetectors with $In_{0.82}Al_{0.18}Sb$ barrier layers were grown on a (100) 6° offcut Si substrate by heteroepitaxy via an AlSb/GaSb buffer. Based on an interfacial misfit array growth mode, the dislocations at the GaSb/Si and InSb/AlSb interfaces accommodated the lattice mismatch. The $In_{0.82}Al_{0.18}Sb$ barrier layer increased the 77 K R_0A of the detector. From 180 K to 300 K, the generation-recombination mechanism dominated the dark current generation in the detector and surface leakage became dominant below 120 K. The detector exhibited a 77 K responsivity of 0.475 A/W and a Johnson-noise-limited detectivity of 3.08×10^9 cmHz$^{1/2}$W^{-1} at 5.3 μm.

OCIS codes: (040.0040) Detectors; (040.3060) Infrared; (230.5170) Photodiodes; (130.3120) Integrated optics devices; (040.6040) Silicon.

References and links

1. A. A. Kosterev and F. K. Tittel, "Chemical sensors based on quantum cascade lasers," IEEE J. Quantum Electron. **38**(6), 582–591 (2002).
2. V. M. Lavchiev and B. Jakoby, "Photonics in the Mid-Infrared: Challenges in Single-Chip Integration and Absorption Sensing," IEEE J. Sel. Top. Quantum Electron. **23**(2), 452 (2017).
3. A. Rogalski, "Infrared detectors: status and trends," Prog. Quantum Electron. **27**(2-3), 59–210 (2003).
4. R. Soref, "Mid-infrared photonics in silicon and germanium," Nat. Photonics **4**(8), 495–497 (2010).
5. A. Spott, E. J. Stanton, N. Volet, J. D. Peters, J. R. Meyer, and J. E. Bowers, "Heterogeneous Integration for Mid-Infrared Silicon Photonics," IEEE J. Sel. Top. Quantum Electron. **23**(6), 1–10 (2017).
6. J. I. Chyi, D. Biswas, S. Iyer, N. Kumar, H. Morkoc, R. Bean, K. Zanio, H. Y. Lee, and H. Chen, "Molecular beam epitaxial growth and characterization of InSb on Si," Appl. Phys. Lett. **54**(11), 1016–1018 (1989).
7. Z.-H. Zhu, F. E. Ejeckam, Y. Qian, J. Zhang, Z. Zhang, G. L. Christenson, and Y. Lo, "Wafer bonding technology and its applications in optoelectronic devices and materials," IEEE J. Sel. Top. Quantum Electron. **3**(3), 927–936 (1997).
8. A. Rogalski, J. Antoszewski, and L. Faraone, "Third-generation infrared photodetector arrays," J. Appl. Phys. **105**(9), 091101 (2009).
9. G. E. Franklin, D. H. Rich, H. Hong, T. Miller, and T. Chiang, "Interface formation and growth of InSb on Si(100)," Phys. Rev. B Condens. Matter **45**(7), 3426–3434 (1992).
10. E. Michel, J. Xu, J. Kim, I. Ferguson, and M. Razeghi, "InSb infrared photodetectors on Si substrates grown by molecular beam epitaxy," IEEE Photonics Technol. Lett. **8**(5), 673–675 (1996).
11. M. Mori, N. Akae, K. Uotani, N. Fujimoto, T. Tambo, and C. Tatsuyama, "Heteroepitaxial growth of InSb films on a Si (001) substrate via AlSb buffer layer," Appl. Surf. Sci. **216**(1-4), 569–574 (2003).
12. G. Balakrishnan, S. Huang, L. Dawson, Y.-C. Xin, P. Conlin, and D. Huffaker, "Growth mechanisms of highly mismatched AlSb on a Si substrate," Appl. Phys. Lett. **86**(3), 034105 (2005).
13. S. H. Huang, G. Balakrishnan, A. Khoshakhlagh, L. R. Dawson, and D. L. Huffaker, "Simultaneous interfacial misfit array formation and antiphase domain suppression on miscut silicon substrate," Appl. Phys. Lett. **93**(7), 071102 (2008).
14. S. Woo, S. Hosseini Vajargah, S. Ghanad-Tavakoli, R. Kleiman, and G. Botton, "Direct observation of anti-phase boundaries in heteroepitaxy of GaSb thin films grown on Si (001) by transmission electron microscopy," J. Appl. Phys. **112**(7), 074306 (2012).
15. T. Grassman, M. Brenner, S. Rajagopalan, R. Unocic, R. Dehoff, M. Mills, H. Fraser, and S. Ringel, "Control and elimination of nucleation-related defects in GaP/Si (001) heteroepitaxy," Appl. Phys. Lett. **94**(23), 232106 (2009).

#320121 https://doi.org/10.1364/OE.26.007227
Journal © 2018 Received 18 Jan 2018; revised 28 Feb 2018; accepted 5 Mar 2018; published 9 Mar 2018

16. G. Savich, J. Pedrazzani, D. Sidor, S. Maimon, and G. Wicks, "Dark current filtering in unipolar barrier infrared detectors," Appl. Phys. Lett. **99**(12), 121112 (2011).
17. K. Ueno, E. G. Camargo, T. Katsumata, H. Goto, N. Kuze, Y. Kangawa, and K. Kakimoto, "InSb mid-infrared photon detector for room-temperature operation," Jpn. J. Appl. Phys. **52**(9R), 092202 (2013).
18. S. Fang, K. Adomi, S. Iyer, H. Morkoc, H. Zabel, C. Choi, and N. Otsuka, "Gallium arsenide and other compound semiconductors on silicon," J. Appl. Phys. **68**(7), R31–R58 (1990).
19. Y. Kim, J. Lee, Y. Noh, M. Kim, Y. Kwon, J. Oh, and R. Gronsky, "Effect of two-step growth on the heteroepitaxial growth of InSb thin film on Si (001) substrate: A transmission electron microscopy study," Appl. Phys. Lett. **89**(3), 031919 (2006).
20. M. De Giorgi, A. Taurino, A. Passaseo, M. Catalano, and R. Cingolani, "Interpretation of phase and strain contrast of TEM images of $In_xGa_{1-x}As/GaAs$ quantum dots," Phys. Rev. B **63**(24), 245302 (2001).
21. B. W. Jia, K. H. Tan, W. K. Loke, S. Wicaksono, and S. F. Yoon, "Epitaxial growth of low threading dislocation density InSb on GaAs using self-assembled periodic interfacial misfit dislocations," Mater. Lett. **158**, 258–261 (2015).
22. Y. Wang, P. Ruterana, S. Kret, S. El Kazzi, L. Desplanque, and X. Wallart, "The source of the threading dislocation in GaSb/GaAs hetero-structures and their propagation mechanism," Appl. Phys. Lett. **102**, 052102 (2013).
23. D. M. Hwang, S. A. Schwarz, T. S. Ravi, R. Bhat, and C. Y. Chen, "Strained-layer relaxation in fcc structures via the generation of partial dislocations," Phys. Rev. Lett. **66**(6), 739–742 (1991).
24. V. Pusino, C. Xie, A. Khalid, M. J. Steer, M. Sorel, I. G. Thayne, and D. R. Cumming, "InSb Photodiodes for Monolithic Active Focal Plane Arrays on GaAs Substrates," IEEE Trans. Electron Dev. **63**(8), 3135–3142 (2016).
25. A. Rogalski, K. Adamiec, and J. Rutkowski, *Narrow-gap Semiconductor Photodiodes* (SPIE Press, 2000).
26. W. Hu, X. Chen, F. Yin, Z. Quan, Z. Ye, X. Hu, Z. Li, and W. Lu, "Analysis of temperature dependence of dark current mechanisms for long-wavelength HgCdTe photovoltaic infrared detectors," J. Appl. Phys. **105**(10), 104502 (2009).
27. C. E. Jones, V. Nair, and D. L. Polla, "Generation-recombination centers in p-type $Hg_{1-x}Cd_xTe$," Appl. Phys. Lett. **39**(3), 248–250 (1981).
28. M. Erkus, O. Senel, and U. Serincan, "Structural, optical and electrical characterization of $InAs_{0.83}Sb_{0.17}$ p-π-n photodetector grown on GaAs substrate," Thin Solid Films **616**, 141–144 (2016).
29. W. Tennant, ""Rule 07" revisited: Still a good heuristic predictor of p/n HgCdTe photodiode performance?" J. Electron. Mater. **39**(7), 1030–1035 (2010).
30. B. R. Conley, J. Margetis, W. Du, H. Tran, A. Mosleh, S. A. Ghetmiri, J. Tolle, G. Sun, R. Soref, B. Li, H. A. Naseem, and S.-Q. Yu, "Si based GeSn photoconductors with a 1.63 A/W peak responsivity and a 2.4 μm long-wavelength cutoff," Appl. Phys. Lett. **105**(22), 221117 (2014).
31. F. Fuchs, U. Weimer, W. Pletschen, J. Schmitz, E. Ahlswede, M. Walther, J. Wagner, and P. Koidl, "High performance $InAs/Ga_{1-x}In_xSb$ superlattice infrared photodiodes," Appl. Phys. Lett. **71**(22), 3251–3253 (1997).
32. A. Evirgen, J. Abautret, J. Perez, A. Cordat, A. Nedelcu, and P. Christol, "Midwave infrared InSb nBn photodetector," Electron. Lett. **50**(20), 1472–1473 (2014).
33. A. Tevke, C. Besikci, C. Van Hoof, and G. Borghs, "InSb infrared p–i–n photodetectors grown on GaAs coated Si substrates by molecular beam epitaxy," Solid-State Electron. **42**(6), 1039–1044 (1998).
34. Z. Djuric, B. Livada, V. Jovic, M. Smiljanic, M. Matic, and Z. Lazic, "Quantum efficiency and responsivity of InSb photodiodes utilizing the Moss-Burstein effect," Infrared Phys. **29**(1), 1–7 (1989).

1. Introduction

Photonic spectrum at the mid-infrared (MIR) region (3-8 μm) reveals information about some important chemical molecules, such as CO_2, H_2O, CH_4, NH_3, –OH, and –CH. Therefore, mid-infrared photodetectors have been used widely in environmental monitoring, automotive industry, food science, and medicine [1–3]. InSb is an attractive material for MIR photodetectors due to its 300 K bandgap of 0.17 eV, robust chemical properties, mature growth, and fabrication techniques [3]. Integration of InSb photodetectors on Si could be an essential step for the next generation of InSb focal plane arrays (FPAs) [3]. Moreover, InSb photodetectors on Si could also play an important role in MIR silicon photonics where the devices on Si platforms operate in the MIR region. MIR silicon photonics provide a higher channel density for on-chip optical interconnects and are also crucial for on-chip chemical and biological sensors [4, 5].

Strategies to integrate InSb photodetectors on a Si platform have been proposed to overcome their large lattice mismatch (19.3%). They can be generally categorized into heteroepitaxial growth [6], wafer bonding [7], and the flip-chip package [3]. Heteroepitaxial growth of an InSb layer on a (100) Si substrate not only overcomes the limit of small-sized

Optics EXPRESS

InSb substrates in the wafer bonding, it also helps to reduce the complicity of fabrication in the flip-flop package where sophisticated substrate thinning and alignment processes are required to integrate small InSb pixels on Si [8]. Directly depositing In and Sb atoms on (100) Si results in the formation of In metallic balls instead of a continuous InSb layer because of the preference of Sb to chemically bond with Si rather than In [9]. Therefore, an intermediate buffer between InSb and Si is required. GaAs has been used as a buffer to grow InSb photodetectors on (100) Si substrates due to its small lattice mismatch with Si [6, 10]. Compared with GaAs, the lattice mismatch between GaSb or AlSb and InSb is even smaller (6.28%). Applying an AlSb buffer for the growth of InSb on GaAs and Si has been reported in previous studies [11]. However, the direct growth of AlSb on Si resulted in lattice rotation [12]. Intentionally forming an interfacial misfit (IMF) array at the GaSb/Si interface is a novel approach to grow low-defect GaSb on Si [13], where uniformly distributed 90° misfit dislocations accommodate the lattice mismatch. Moreover, the misalignment between III-V compound semiconductors (polar structure) and Si (non-polar structure) resulted in the formation of anti-phase boundary (APB) in III-V compound semiconductors [14]. This challenge can be tackled using offcut Si substrate due to double-atomic-height steps forming on the surface of offcut Si substrate [13, 15].

In this work, we demonstrated the heteroepitaxial growth of the InSb p-i-n photodetector on a (100) 6° offcut Si substrate via a 250-nm-thick AlSb/GaSb buffer. The lattice mismatch between GaSb and Si was accommodated by the IMF array. An electron barrier $In_{0.82}Al_{0.18}Sb$ layer was inserted into the photodetector to suppress the dark current [16]. $In_{0.82}Al_{0.18}Sb$ has a large conduction band offset (0.54 eV at 77 K) and a negligible valence band offset (nearly 0 eV at 77 K) with InSb [17]. The InSb photodetector on Si exhibited a 77 K Johnson-noise-limited detectivity of 3.08×10^9 $cmHz^{1/2}W^{-1}$.

2. Experimental procedures

The epitaxy structure of the InSb p-i-n photodetector with an $In_{0.82}Al_{0.18}Sb$ barrier layer on Si is shown in Fig. 1(a). The entire growth process was carried out using a solid-state molecular beam epitaxy (MBE). The n-type and p-type dopant was Si and Be, respectively. Before the growth, the (100) 6° offcut Si substrate was etched with hydrofluoric acid to remove surface oxide. Then it was transferred to the MBE system and heated up to 950 °C for 30 mins to form double layer steps on the Si surface, which is essential for the suppression of APB in compound semiconductors on Si [18]. A 5 nm AlSb prelayer was first grown on Si at 560 °C. A spotty reflection high-energy electron diffraction (RHEED) pattern was observed, which indicated the formation of AlSb islands on the Si surface. Subsequently, a 200 nm GaSb layer and a 50 nm AlSb layer were grown at 430 °C. A 100 nm InSb buffer was grown on AlSb at 310 °C, because the lower growth temperature of InSb on AlSb promoted the formation of 90° misfit dislocations at their interface [19]. Finally, the structure of the InSb photodetector was grown on the AlSb surface at 345 °C. An $In_{0.82}Al_{0.18}Sb$ barrier layer was also grown at 345 °C. In and Al fluxes were calibrated using the MBE flux gauge to determine the composition of the $In_{0.82}Al_{0.18}Sb$ layer.

In the InSb photodetector device fabrication, an InSb mesa was formed on each photodetector using a wet etch process with an etchant solution composed of citric acid and H_2O_2 (the ratio of citric acid and H_2O_2 = 33:2 by weight). The mesa areas ranged from 0.228 mm^2 to 0.00145 mm^2. Au (150 nm)/Ti (30 nm) contacts were formed at the n + and p + contact layers, respectively, using the standard electron beam evaporation technique. No surface passivation or antireflection coating was applied on these devices. The InSb photodetectors were mounted in a liquid nitrogen cooled optical cryostage for the characterization from 77 K to 300 K. The photoresponse of the InSb detector was measured using a 700 °C black body and a MIR tunable laser as the light source.

Optics EXPRESS

3. Results and discussion

Figure 1(b) shows an X-ray diffraction (XRD) (004) *ω-2θ* scan of the InSb photodetector grown on Si via the AlSb/GaSb buffer. The peaks of InSb, InAlSb, AlSb, GaSb, and Si are indicated in the figure. Figure 1(c) contains a (115) XRD reciprocal space map (RSM) of the sample. The diagonal dashed line indicates fully relaxed layers on Si. The centers of the InSb and GaSb peaks are located along the line, which indicates that the InSb and GaSb layers are nearly fully relaxed. Using the data from Fig. 1(b) and (c), the degrees of relaxation in the GaSb buffer and InSb layer were calculated to be 99.5% and 99.2%, respectively. Above the InSb peak, a weak x-ray signal with a smaller Q_z than the InSb peak was observed, which could be attributed to the $In_{0.82}Al_{0.18}Sb$ barrier layer. The same Q_x of InSb and $In_{0.82}Al_{0.18}Sb$ suggested that the $In_{0.82}Al_{0.18}Sb$ is fully tensile-strained with InSb.

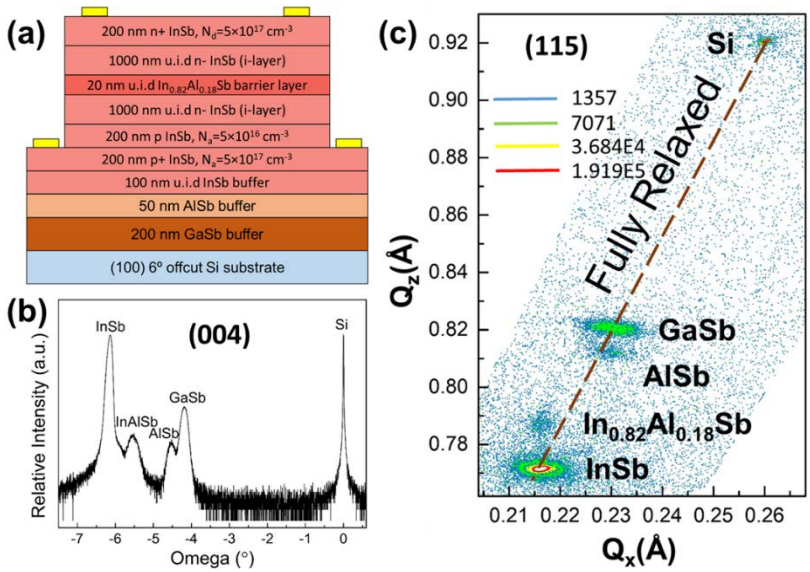

Fig. 1. (a) Schematic diagram of the InSb p-i-n photodetector with an $In_{0.82}Al_{0.18}Sb$ barrier layer grown on a (100) 6° offcut Si substrate via a 250-nm-thick AlSb/GaSb buffer. (b) (004) XRD *ω-2θ* scan of the InSb photodetector grown on Si. (c) (115)XRD space map (RSM) of the InSb photodetector grown on Si.

Figure 2(a) contains a bright-field transmission electron microscopy (TEM) image of the GaSb/Si interface. The interface is abrupt and misfit dislocations are uniformly distributed along it, which indicates an IMF array. No APB is observed. Figure 2(b) shows the HR TEM image of the IMF array at the GaSb/Si interface where periodically distributed dark and light bands are observed. These bands are attributed to the strain fields around interfacial misfit dislocations [20] and are the feature of an IMF array. The lattice mismatch between GaSb and Si is accommodated by uniformly distributed 90° misfit dislocations [13, 21]. The bright-field image of the InSb/AlSb interface is shown in Fig. 2(c). Unlike the GaSb/Si interface, some dark regions distributes irregularly along the InSb/AlSb interface. These dark regions are caused by interfacial misfit dislocations.

Optics EXPRESS

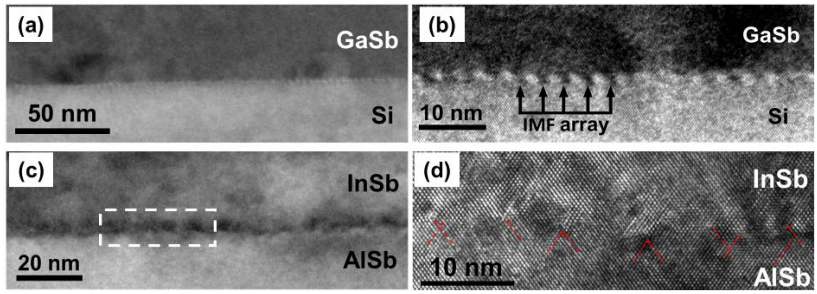

Fig. 2. (a) Bright-field TEM image of the GaSb/Si interface. (b) High resolution TEM (HR TEM) image of an IMF array at the GaSb/Si interface. (c) Bright-field TEM image of the InSb/AlSb interface. (d) HR-TEM image of the misfit dislocations obtained in the dashed box in (c). 60° misfit dislocations are indicated by one arrow and 90° misfit dislocations are indicated by a pair of arrows.

To investigate the InSb/AlSb interface further, a HR-TEM image was acquired of the dashed box region in Fig. 2(c), as shown in Fig. 2(d). The extra lattice plane is indicated by a red dashed arrow. 90° misfit dislocations, which are associated with two extra lattice planes, are marked by a pair of arrows, while 60° misfit dislocations, which are associated with one extra lattice plane, are marked by a single arrow. Two 90° misfit dislocations and seven 60° misfit dislocations were observed. Unlike the 90° misfit dislocations, the 60° dislocations glided along the (111) lattice plane to form threading dislocations [22]. There was no uniformly distributed 90° misfit dislocation array at the InSb/AlSb interface. Six of the 60° misfit dislocations were located close to another 60° misfit dislocation. Two adjacent 60° misfit dislocations may annihilate each other during propagation to suppress the formation of a threading dislocation [23].

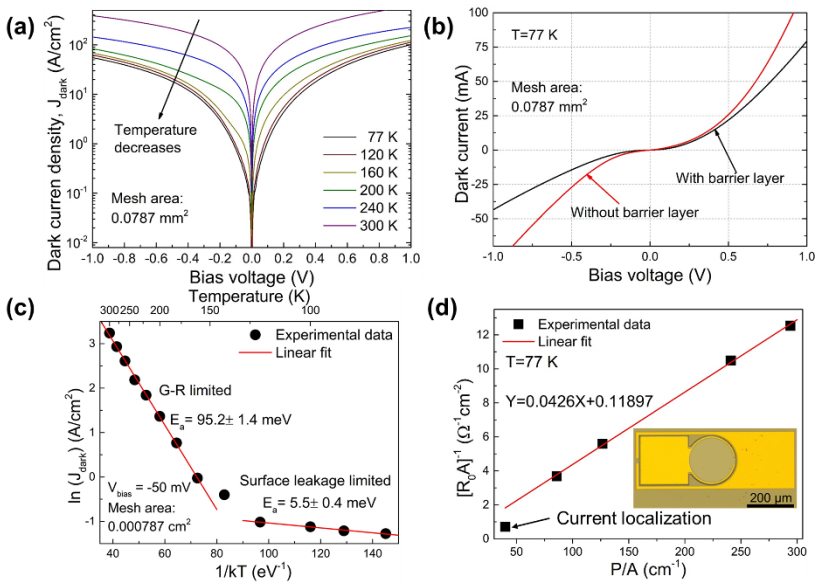

Fig. 3. (a) Temperature dependent dark current density (J_{dark})-voltage curves temperature for the detector with a mesa area of 0.0787 mm^2. (b) Comparison of voltage dependent J_{dark} at 77 K between the InSb photodetector with and without the barrier layer. (c) The natural logarithm of ln(J_{dark}) vs. 1/kT for the device presented in (a) and the red lines are the Arrhenius fitting using Eq. (1) from 300 K to 77 K. (d) Perimeter-to-area (P/A) ratio dependent R_0A for detectors with different sizes at 77 K. The solid lines are the fitting using Eq. (2). The inset is the optical image of the InSb photodetector.

Optics EXPRESS

Figure 3(a) shows the temperature dependent dark current density-bias voltage (J_{dark}-V_{bias}) curves for the detector with a mesa area of 0.0787 mm^2. The J_{dark} increased from 77 K to 300 K. The J_{dark} below 160 K is insensitive to temperature. The 300 K J_{dark} at V_{bias} = −50 mV is 25.49 A/cm^2, which is comparable to the J_{dark} of 27 A/cm^2 reported for the InSb photodetector on GaAs [24]. To identify the effect of the $In_{0.82}Al_{0.18}Sb$ barrier layer on the J_{dark} of InSb photodetectors, a sample without the barrier layer was grown on Si and fabricated. Figure 3(b) compared 77 K dark current-V_{bias} curves between the detectors (with identical mesa sizes) with and without a barrier layer. Zero bias resistance (R_0) is the differential resistance of a p-i-n photodetector at V_{bias} = 0 V which was extracting from dark current-V_{bias} curves. The detector with the barrier layer has a zero bias resistance-area product (R_0A) of 0.179 Ωcm^2, while the detector without the barrier layer has a R_0A of 0.091 Ωcm^2. The effect of a 20 nm $In_{0.82}Al_{0.18}Sb$ barrier layer is comparable to the effect of an InAlSb barrier layer in the InSb detector on GaAs, as the R_0A was increased by 70% due to the barrier layer [17]. Both Fig. 3(a) and (b) show the J_{dark} increases with the increasing reverse bias, especially at V_{bias} below −0.2 V. This phenomenon can be attributed to surface leakage which will be discussed later and carrier tunneling mechanism. For narrow bandgap photodiode, carriers easily tunnel through the PN junction to the other side of the junction at a high reverse bias to form tunnel current [25]. Both surface leakage and tunnel current strongly depend on reverse bias, therefore, its effect is not remarkable under a low or zero reverse bias [26]. The remarkable increment in the tunneling and surface leakage current at a high reverse bias make contribution to the rapidly increasing J_{dark} with the increasing reverse bias. Figure 3(c) shows the temperature dependent J_{dark} at V = −50 mV from 77 K to 300 K to investigate the dark current generating mechanism. The J_{dark} can be fitted using the Arrhenius equation as

$$J_{dark} = J_0 \exp\left(-\frac{E_a}{k_B T}\right) \tag{1}$$

where J_0 is the pre-exponential factor, E_a is the activation energy, k_B is the Boltzmann constant, and T is the temperature. From 300 K to 160 K, E_a is 95.2 meV, which is about half of the InSb band gap in this temperature range. Therefore, the dark current generating mechanism is the generation-recombination (G-R) mechanism where carriers were thermally excited from the valence band to the conduction band via the defects between the two bands [27]. Below 120 K, the E_a decreases to 5.5 meV, which is much lower than the bandgap of InSb. This low activation energy suggests that the dark current generating mechanism in this temperature range could be due to surface leakage [28].

To investigate the surface leakage current at 77 K, the relationship between perimeter-to-area (P/A) ration and the $[R_0A]^{-1}$ was measured and is shown in Fig. 3(d). The P/A dependent $[R_0A]^{-1}$ can be fitted using

$$\frac{1}{R_0A} = \frac{1}{R_0A_{bulk}} + \frac{1}{r_{surface}}\frac{P}{A} \tag{2}$$

where R_0A_{bulk} is the bulk contribution to the R_0A, $r_{surface}$ is the surface resistivity, and P/A is the perimeter-to-area ratio of the detector. The fitted results are shown in Fig. 3(d) where the $r_{surface}$ is 23.47 Ωcm and R_0A_{bulk} is 8.41 Ωcm^2. For the detector shown in Fig. 3(c) with a P/A of 126.6 cm^{-1}, the reciprocal bulk resistivity ($\frac{1}{R_0A_{bulk}}$) is 0.119 $\Omega^{-1}cm^{-2}$ and the item about the reciprocal surface resistivity ($\frac{1}{r_{surface}}\frac{P}{A}$) is 5.394 $\Omega^{-1}cm^{-2}$. The low surface resistivity

Optics EXPRESS

decreases the R_0A. Therefore, the contribution of surface leakage to J_{dark} is remarkable at 77 K, which is consistent with the results in Fig. 3(c).

The surface leakage current could be attributed to surface states. It can be suppressed by applying surface passivation [3]. For the detector with the smallest P/A (i.e. the largest mesa area shown in the bottom right corner of Fig. 3(d)), the surface leakage current does not obey the linear relationship between $[R_0A]^{-1}$ and P/A. This phenomenon could be explained as current localization [24], where the current collection is not efficient. As shown in the inset of Fig. 3(d), the dark current of the InSb detector was collected by the annular top electrode around the mesa. For the detector with a large mesa size, the thermally generated carriers at the center of the mesa were not collected by the annular electrode. Therefore, the measured J_{dark} is lower than the actual generated current: leading to a lower $[R_0A]^{-1}$. Moreover, the analysis of the dark current generating mechanism and P/A dependent $[R_0A]^{-1}$ indicate that the $In_{0.82}Al_{0.18}Sb$ barrier layer only partially blocks the dark current and is not an ideal one. The ideal barrier layer is able to make the R_0A of the detector near "Rule-07" [16]. Rule-07 assumes all dark current is Auger-limited where the 77 K R_0A is 2.29×10^{10} Ω/cm^2 for the detector with the cutoff wavelength of 5.5 μm [29].

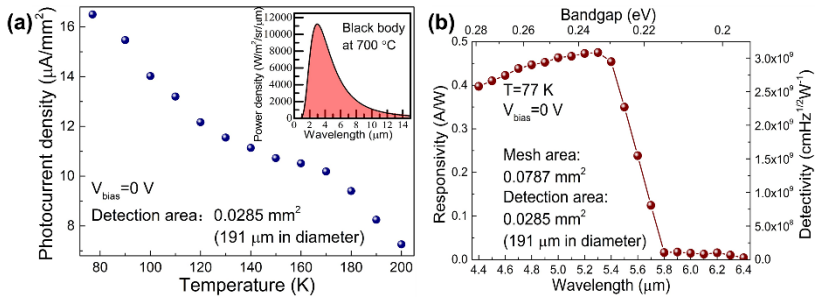

Fig. 4. (a) Temperature-dependent photocurrent density of the InSb detector on Si. The light source is a blackbody maintained at 900 °C and its output spectrum is shown in the inset of (a). (b) Spectral response of the InSb detector on Si. The left and right y-axis is the responsivity and detectivity, respectively.

Figure 4(a) shows the temperature dependent photoresponsivity of the InSb detector on Si. A black body maintained at 700 °C was used as the light source and its output spectrum is shown in the inset of Fig. 4(a). The black body radiation was chopped at 200 Hz. The InSb detector was operated at V_{bias} = 0V (i.e. photovoltaic mode) to minimize the dark current. The measured photocurrent density decreased with an increase in temperature from 77 K to 200 K, which was attributed to a lower carrier lifetime and a higher background carrier concentration at a higher temperature [30]. The 77 K spectra responsivity was measured using a tunable laser from 4.4 μm to 6.4 μm with a step of 0.1 μm and its output intensity was calibrated by a laser power meter. The detector was operated at photovoltaic mode. The detector exhibited a 50% cutoff wavelength of 5.5 μm. The highest responsivity (R_p) was 0.475 A/W obtained at 5.3 μm, which corresponds to a quantum efficiency of 11.1%. Based on the electrical and optical characterization, the Johnson-noise-limited detectivity (D*) of this device was estimated [31] using

$$D^* = R_p \left(\frac{R_0 A}{4 k_B T} \right)^{1/2} \tag{3}$$

where k_B is Boltzmann's constant and T is the 77 K. The D* is also shown in Fig. 4(b) and the highest D* is 3.08×10^9 cmHz$^{1/2}$W^{-1} at 5.3 μm.

The D* of the InSb detector on Si could be further improved for application in a practical system. Optimizing the growth of InSb on AlSb to minimize the formation of 60° interfacial

Optics EXPRESS

misfit dislocations, which lead to threading dislocations, is essential. A high threading dislocation density decreased the R_0A significantly. The R_0A can be increased through optimizing the barrier layer. A 50 nm $In_{1-x}Al_xSb$ graded barrier layer with x varying from 0.15 to 0.35 was inserted in the InSb photoconductor to form an nBn photodetector and to achieve a low 77 K dark current [32]. Increasing the absorption layer (i-layer) thickness to enhance responsivity would be an option. The InSb photodetectors with the i-layer thickness of 6 μm have been grown on GaAs-coated Si substrates. Their highest 77 K responsivity was 1.4 A/W [33] and detectivity was 2.8×10^{10} $cmHz^{1/2}W^{-1}$ [10] which are both higher than that of the InSb detectors presented in this paper. The absorption coefficient of InSb at 5.3 μm is around 3100 cm^{-1} [34]. Therefore, an absorption layer thickness of at least 3.2 μm is needed to absorb (1-1/e) of incident 5.3 μm light.

4. Conclusion

In conclusion, InSb photodetectors with $In_{0.82}Al_{0.18}Sb$ barrier layers grown on a (100) 6° offcut Si substrate via an AlSb/GaSb buffer were investigated. The misfit dislocations at the GaSb/Si and InSb/AlSb interfaces accommodated the lattice mismatch between InSb and Si and minimized the formation of defects in the InSb layer. The $In_{0.82}Al_{0.18}Sb$ barrier layer increased the R_0A of the InSb detector by 96.7%. It is suggested that the dark current of the InSb detector is generated by the G-R mechanism from 160 K to 300 K and by surface leakage below 120 K. At 77 K, the detector obtained a 77 K responsivity of 0.475 A/W at 5.3 μm, which corresponded to a Johnson-noise-limited detectivity of 3.08×10^9 $cmHz^{1/2}W^{-1}$. With further optimization, this InSb detector grown on Si could be applied in InSb FPA and MIR silicon photonics.

Funding

Singapore National Research Foundation through the Competitive Research Program (Grant No: NRF-CRP6-2010-4).